Processing-Induced Changes in the Local Structure of Amorphous Polyaniline by Radial Distribution Function Analysis of X-ray Scattering Data

J. Maron[†] and M. J. Winokur*

Department of Physics, University of Wisconsin, Madison, Wisconsin 53706

B. R. Mattes

Los Alamos National Laboratory, Los Alamos, New Mexico 87545

Received September 23, 1994; Revised Manuscript Received March 15, 1995[⊗]

ABSTRACT: The local molecular structure of amorphous polyaniline (PANI) film in the emeraldine oxidation state has been studied using radial distribution function analysis of X-ray scattering data in combination with model calculations. As-cast emeraldine base (EB) films exhibit an interchain ordering that is significantly poorer than that for the intrachain structure. Protonic acid (HBr or HCl) doping of these films, to yield the electrically conductive emeraldine salt (ES) form of PANI, leads to significant changes in both the intrachain and interchain structure of the polymer chains. Structural changes in the *intrachain* ordering are found to be essentially reversible on undoping since, after all of the dopant is removed from ES films by immersion in a strong base solution, the original as-cast EB intrachain features become more pronounced. In contrast, evidence of irreversible changes in the *interchain* packing is observed during this doping/undoping process following the treatment with base. These changes in the EB local molecular ordering may be intimately coupled to the electronic properties intrinsic to conducting polymers and they occur in such a way that subsequent exposure to protonic acids initiates a highly site-specific redoping of the polymer host. These findings shed light on the doping-induced variations of the physical properties in conducting polymers such as charge and mass transport through polyaniline films.

I. Introduction

The nature of a polymer's microscopic molecular organization is a central issue in many fundamental and applied studies. Polymer films and coatings are frequently anisotropic, and their final properties are often quite sensitive to both synthesis and processing conditions. Polymers are processed to give thermodynamically metastable states, i.e., rubber, glass, or semicrystalline phases, primarily as a function of forming temperature. The nature of the final film structure and physical properties rigorously depend upon film formation conditions such as polymer molecular weight, solvent selection, solution viscosity, etc. For instance, the gas transport properties of polymers which serve as useful gas-selective barriers vary greatly depending on their state: rubbery polymers exhibit high rates of gas flux with low selectivities, while the inverse is true for most of the glassy polymers.[1] These or other structure/property relationships, such as mass or charge transport through conducting polymers, are better understood in terms of both intrachain and interchain structural ordering.

In primarily crystalline (or semicrystalline) hosts, well-defined periodicities exist to a sufficient extent that classical Bragg scattering techniques[2] may be applied. However, detailed structure factor calculations often yield an incomplete set of information concerning either the intrachain or interchain ordering due to the limited number of unique Bragg reflections that are typically resolved. A related technique for studying the local structural order is radial distribution function (RDF) analysis[3–5] of X-ray or neutron scattering data. One notable advantage of the RDF methodology is that it may be applied to systems regardless of the degree of crystallinity.[6] This method yields precise information for the smallest intra- and interchain distances and, when utilized in conjunction with modeling techniques, can shed light on amorphous polymer structure. In pure, single-element materials RDF analysis yields the element-specific pair distribution function. For multielement systems such as polymers, the RDF curve represents a weighted sum of atom–atom pair distributions.

RDF studies have been reported for a host of conventional polymers[7] (e.g., nylon-6,[6] polyethylene,[8,9] and poly(ethylene oxide)[10] and one conducting polymer system (i.e., polyaniline[11–13]). Most of these host systems possess relatively simple monomer repeat units with well-defined chemical bonds forming the polymer chain. These bonding features tend to dominate the RDF spectra, especially at length scales which correspond to nearest-neighbor or next-nearest-neighbor distances (from 1.3 to 2.5 Å). The RDF features appearing at somewhat longer length scales can be sensitive to both the intersegmental chain conformations and the packing structure adopted by neighboring polymer chains. This fact makes it difficult to quantitatively assess the precise origins of these RDF contributions. Still, the linked-atom structural modeling techniques that are routinely used for crystallographic studies of polymers[14–16] may also be applied to RDF analysis of amorphous polymers to deduce qualitative and quantitative structural information.

In this paper we present a combined RDF/linked-atom modeling analysis approach in order to more fully investigate the short-range intrachain and interchain chain structure in various forms of amorphous polyaniline (PANI). These results indicate that intrachain ordering always dominates the RDF spectra at the

[†] Current address: Department of Physics, California Institute of Technology, Pasadena, CA 91125.

[⊗] Abstract published in *Advance ACS Abstracts,* May 1, 1995.

0024-9297/95/2228-4475$09.00/0

shortest length scales (typically 5 Å or less). As-cast PANI films are found to exhibit rather poor interchain ordering. Direct comparisons with selected RDF model spectra show that the undoped films (as-cast or cycled) have structures that are consistent with the conventional model whereby three benzenoid (B) phenylene rings alternate with one quinoidal (Q) unit (or BBQB). Protonic acid doping is found to have a profound influence on both the local interchain and intrachain structure. After a full doping cycle, protonic acid doping followed by undoping with 1 M NH_4OH, there is evidence for reversibility with respect to the intrachain structure but permanent changes occur within the interchain chain packing. The existence of this irreversibility is central to a proposed model which may partially explain the microscopic origins of the pronounced selectivity enhancement seen in gas diffusion studies of protonic acid redoped films.[17]

II. Polyaniline

Polyaniline is a member of the family of conducting polymers which are valued for their unique electronic and optical properties.[18-20] PANI can be prepared as a thin film or powder by either electrochemical methods[21] or direct chemical synthetic routes.[22-24] The chemical formula which most broadly describes this polymer is represented by

$$([(-C_6H_4-NH-C_6H_4-NH-)_{1-x}][(-C_6H_4-N=C_6H_4=N-)_x])_n$$

PANI may be prepared in a number of different oxidation states[25,26] ranging from the fully oxidized ($x = 1$) pernigraniline form to the fully reduced ($x = 0$) leucoemeraldine form. Certain types of these PANI compositions, e.g., leucoemeraldine, are amenable to n- or p-type doping which imparts electrical conductivity to them.[27] Emeraldine is easily processed[28,29] by solution- or melt-processing techniques to give useful articles such as fibers, films, and coatings that are also electronically conducting. Examples of potential applications for such polyaniline-based articles are summarized in ref 30.

The present study is only concerned with PANI when prepared by chemical synthesis to yield the polymer in what is known as the emeraldine[26] oxidation state ($x = 0.5$) or emeraldine base (EB). This form of PANI is characterized by a four-monomer chain repeat and it is unique because simple acid-base chemistry can be employed to control the physical and structural properties of the polymer. For instance, the dc electrical conductivity of emeraldine powder can be selectively tailored from 10^{-10} to 10^{+1} S/cm by varying the number of available protonation sites as a function of exposure to an equilibrium pH of an acid.[31,32] Similarly, the gas transport properties of EB films can be controlled as a function of the extent of doping with an acid to give highly selective membranes that allow for faster rates of transport for small gases compared with the larger gases in a mixture.[17,33-35] This process is sensitive to both the dopant concentration and the size of the dopant solvation sphere.

Figure 1 shows the reversible nature of the protonic acid doping and undoping of emeraldine using a protonic acid (HX). Protonation of emeraldine base (EB in Figure 1a) occurs preferentially at the imine nitrogen atoms[36] to form an emeraldine salt (ES). Percent doping (y) is thereby calculated for emeraldine salts from the elemental ratio $y = X^-/N$[37] which is determined from

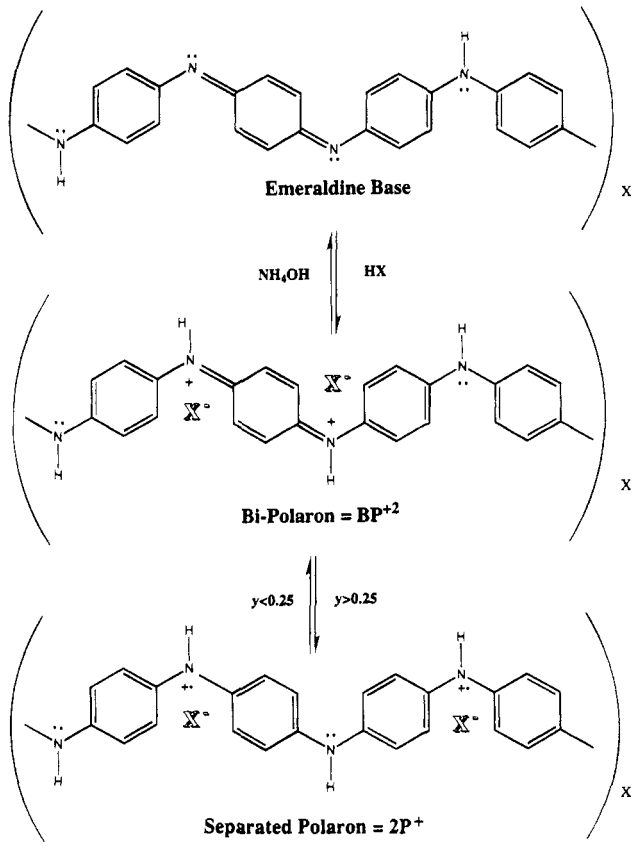

Figure 1. Schematic drawings for (a) emeraldine base, (b) emeraldine salt in theorized bipolaron form, and (c) emeraldine salt in theorized polaron form.

elemental combustion analysis. Fully doped emeraldine has the value $y = 0.5$ since only half the nitrogens are available sites for protonation. Intermediate doping levels, i.e., $y < 0.5$, have doping values that depend upon the equilibrium concentration of an acid in which emeraldine is immersed.

A number of studies have provided evidence for the formation of bipolarons and polarons, depending on the extent of acid doping, to explain the charge transport behavior of emeraldine.[38,39] Figures 1b and 1c illustrate the two proposed emeraldine salt structures for the doped polymer. ES exhibits spinless bipolaron (BP^{2+}) charge carriers[38,39] at doping levels of $y < 0.25$. At higher doping levels, $y > 0.25$, the polymer reorganizes into two separate polarons ($2P^+$) by means of an internal redox mechanism[40,41] as illustrated in Figure 1c. This dopant-induced bipolaron to polaron transition is attributed to Coulombic repulsions that lead to enhanced resonance energy stabilization. An interchain quasi-one-dimensional variable-range hopping mechanism has been proposed to explain charge transport in doped emeraldine compositions.[42]

Coherent free-standing EB films can be prepared by solution-casting techniques.[17,39] The microstructural details of such films are highly sensitive to film formation procedures. Pouget et al.[43] reported the first evidence for multiple lattice phases occurring at differing dopant concentrations. Their as-cast EB-II films (the II refers to casting from the EB form, i.e. $y = 0$) may be up to 5% crystalline, as determined by X-ray diffraction measurements, and this crystalline fraction may increase somewhat as the films are stretch oriented.[44,45] A distinctly different lattice structure evolves in films after fully doping the as-cast EB film with HCl

$y = 0.5$. If the fully doped ES film is treated with aqueous NH_4OH, then the resulting EB film ($y = 0$) always becomes completely amorphous to recover the EB-II form of PANI.[43] After the undoped film is redoped to give emeraldine hydrochloride compositions in the percentage doping ranges between $0 < y < 0.25$, it too is similarly found to be noncrystalline and amorphous. However, at redoping levels which give $y > 0.25$, the original crystalline lattice structure of the fully doped film reappears with diffraction lines increasing in intensity as a function of EB film immersion in decreasing equilibrium pH.

III. Experimental Details

Materials. Aniline [$C_6H_5NH_2$, (Mallinckrodt, St. Louis, MO)] was fractionally distilled in vacuo from barium oxide (5 mmHg, bp range 73–82 °C). Ammonium peroxydisulfate ($NH_4S_2O_8$), 1-methyl-2-pyrrolidinone [NMP, $(CH_3)NC_4H_6O$], and pyrrolidine (C_4H_9N) were used as purchased from Aldrich Chemical Co., Milwaukee, WI. Ammonium hydroxide, 29% by weight [NH_4OH, (Mallinckrodt, St. Louis, MO)], was used as purchased. Tetrahydrofuran (THF) [C_4H_4O, Fisher Scientific, Fair Lawn, NJ] was dried with sodium benzophenone and vacuum distilled prior to use. Hydrochloric (HCl) and hydrobromic (HBr) acids (38%) were used as purchased from Aldrich Chemical Co.

Synthesis of Polyaniline Powder in the Emeraldine Oxidation State. A solution 1 N in HCl was prepared by adding 491.7 g of concentrated HCl to a 5 L volumetric flask and filling to the mark with distilled deionized water. Then 1425 mL of this acid solution was placed into a 3000 mL polymerization vessel along with 122.7 g (1.32 mol) of distilled aniline and maintained with stirring at 3 °C. In a separate flask, 1575 mL of 1 M HCl was combined with 69.03 g (0.303 mol) of ammonium peroxidisulfate. This mixture was stirred until all of the oxidant dissolved and then cooled to 0 °C in a freezer. The persulfate solution was slowly added dropwise to the aniline solution by means of an addition funnel over the course of 60 min. The combined solutions reacted for an additional 3.5 h. The green emeraldine hydrochloride precipitate was collected in a large Büchner funnel. The powder was extracted first in water and then in methanol until the wash solutions were colorless and finally filtered. This as-synthesized polyemeraldine hydrochloride salt was subsequently immersed in 5 L of 0.1 M NH_4OH for 3 h, filtered, and then washed once again with THF and methanol until the solutions were clear. The yield was calculated at 24%. The purified emeraldine base was vacuum dried ($<10^{-5}$ torr) and stored in a vacuum desiccator for further use. Four point probe dc conductivity measurements of a vacuum-dried pressed EB powder after immersion in 4 M HCl for 24 h to form the fully doped ES yielded 1.2 S/cm.

Preparation of Emeraldine Base Films. A 10.8% (w/w) solution was made as follows: 2.0 g of EB powder was placed in a mortar and pestle and ground to a fine powder, and then added incrementally to a mixture of 16 mL of NMP and 0.6 mL of pyrrolidine. The solution was covered and placed on a hot plate at 60 °C for 30 min. The resulting homogenous solution was free of particles and it remained stable without gelation for weeks. Films were formed on glass plates by means of a gardener blade and annealed at 125 °C for 3 h with an oven purge stream of argon gas. The as-cast films were removed from the plates by immersing them in a distilled water bath. They were extracted in methanol for 48 h to remove residual casting solvent. The as-cast EB films were immersed in either 4 M HCl or 1 M HBr, respectively, for 48 h to give a fully doped membrane. The fully doped films were immersed in a 0.1 M NH_4OH solution for 48 h to give the undoped (cycled) film. These films were dried on a vacuum line ($<10^{-5}$ torr) for 48 h after each chemical treatment. An undoped membrane was once again doped, sequentially, first in a 0.015 M HCl solution and then in a 0.0175 M HCl solution to form the redoped membrane. Drying of the redoped films was performed at ~100 °C in air. In all cases the halogen composition, y, was assumed to closely follow those of the similarly prepared samples employed in ref 17.

RDF Experimental Setup. The experiment was performed on the X7A beamline at the National Synchrotron Light Source operated by Brookhaven National Laboratory. A monochromatic beam of X-rays (typically 1 mm × 10 mm in cross-sectional area) was incident on tightly clamped multilayer stacks of the PANI films. The overall thickness was determined by the availability of sample and the net attenuation by the main beam. Typical samples consisted of 5–25 stacked layers of the various PANI films with a nominal 6 mm × 20 mm × 20 μm dimension for a single layer. Transmission coefficients, as measured directly in the main beam, ranged from approximately 0.70 to 0.95. For this study the samples were mounted using a symmetrical transmission geometry in combination with standard $\theta-2\theta$ scans. Scattering data were acquired from 2θ angles ranging from 5 to 130° in constant 0.1 $Å^{-1}$ steps. In order to maximize the momentum transfer (or q-range) available, the incident photon energy was typically fixed at 0.502 Å. Absorption due to air was negligible but there was appreciable air scatter at low angles which could be minimized by mounting the sample inside a helium-filled Kapton-windowed canister.

The scattered photons were collimated using a pair of rectangular slits adjusted so that a 3 mm × 12 mm aperture existed at the detector orifice. All scattering data were detected using a germanium-based energy-dispersive detector. The total number of counts at each q vector depended on the specific details (i.e., data collection time, beam intensity, etc.) and varied between 10^4 and 10^5 counts. In general, the data collection times were significantly extended at high q to compensate for the reduction in the overall scattering intensity and the increased proportion of Compton scattering. The displayed data have not been smoothed in any way so that the point-to-point fluctuations of the experimental curves are nominally representative of the statistical uncertainties.[46]

The data reduction and analysis closely followed the procedures outlined in Klug and Alexander.[4] All of the experimental data have been corrected for beam intensity fluctuations, detector dead time, sample geometry, attenuation, partial polarization, and incoherent scattering.[47] Normalization of the experimental data to the theoretical profiles was accomplished by using the analytical expression of Krogh-Moe.[48] The large 2θ angles employed in this study, when combined with the transmission geometry and the sample-specific geometrical distortions (that resulted from the clamped mounting procedure), did, at times, introduce a degree of anomalous behavior in the overall functionality in the various curves at the higher q values. These effects could be compensated for using either of two methods: arbitrarily adding a weak quadratic background or by examining systematic failings of the data, at high q, and then applying a somewhat higher order correction. As a general rule the integrated deviation of the experimental curve from that of the theoretical curve, at high q, should ultimately approach zero on average. Both of these ad hoc procedures utilize *slowly* varying functions which introduce new RDF artifacts at very small r values (typically well under 1 Å). The most critical aspect of this whole process is to match the high-q functionalities of the experimental and theoretical curves so that unacceptable truncation effects are not inadvertently introduced. Klug and Alexander[4] provide an extensive overview to the pitfalls inherent in the RDF analysis procedure.

In some cases it was possible to fit the entire energy-dispersed spectra at high q to a composite function so that the elastic scattering components could be extracted and then spliced to the data at lower q. Statistically significant oscillations are observed out well beyond 16 $Å^{-1}$. The most pronounced of these oscillations arise from the well-defined covalent bonding which comprises the polymer backbone. Additional features may arise from the ordering which accompanies the relatively stiff π-conjugated backbone. The persistence of these oscillations out to high q necessarily complicates the data truncation prior to Fourier transformation. An abrupt truncation of the experimental data at some arbitrary momentum transfer will generate strong low-r

artifacts which then, in turn, modify the weaker features at shorter distances. Alternatively, a simple high-q damping of the data may be enforced. This produces RDF features at low r which are artificially broadened and hence more poorly resolved. To minimize these effects we employed a composite scheme in which the experimental data are smoothly spliced to the "calculated" structure function containing only neighboring atom−atom intrachain spacings[49] (for distances less than 3 Å). A Fermi function was used to generate an approximate 3 $Å^{-1}$ overlap region and this process produced a relatively smooth crossover between the two curves. This composite profile was found to retain $qH(q)$ oscillations which extended out to 40 $Å^{-1}$. The net effect of this procedure is to reduce the presence of oscillatory artifacts, especially at low to intermediate r, and to artificially narrow and normalize the relative intensities of the 1.4 and 2.4 Å RDF peaks to values representative of the real polymer pair correlations. Clearly, better experimental data at high momentum transfer will be the best solution. In addition to the various truncation artifacts, there are systematic errors introduced by normalization of the experimental data. There are also systematic problems attributable to the approximations used in analyzing the experimental data and/or in the details of the theoretical analysis (e.g., the explicit form of the Breit−Dirac recoil factor). These effects often appear as artifacts at low r (2.5 Å or less) although there are anomalies which may appear at the larger length scales.[4]

IV. Radial Distribution Function Theory

A. Conventional RDF Analysis. The general form of the coherent scattering intensity originating from a group of atoms in a host system manifesting a readily identifiable structural base unit[2] is given by

$$(I(q))_{\text{unit cell}} = I(q) = \sum_m \sum_n f_m(q) f_n(q) \frac{\sin(kr_{mn})}{kr_{mn}} \qquad (1)$$

where the sum m ranges over atoms in the unit cell (either two or four PANI monomer units) and the sum n ranges over all atoms in the entire sample. The various terms, $f_m(q)$, r_{mn}, and $q = (4\pi/\lambda)\sin\theta$, represent the mth atom structure factor, the distance between atoms m and n, and the momentum transfer of the scattered photons, respectively. This expression can be further modified by separating out the atomic self-scattering terms, $S_s(q)$ (where $m = n$). For halogenic acid-doped PANI there are four element-specific terms (i.e., hydrogen, H; carbon, C; nitrogen, N; and halogen, X) so that

$$I(q) = S_s + \sum_m f_m(q) \sum_{n \neq m} f_n(q) \frac{\sin(qr_{mn})}{qr_{mn}} \qquad (2)$$

where $S_s = c_C f_C^2(q) + c_N f_N^2(q) + c_X f_X^2(q) + c_H f_H^2(q)$ and c_H, c_C, c_N, and c_X are the respective atomic concentrations in the chosen base model cell. This discrete sum must now be transformed into an integral expression in terms of the continuous pair distribution functions, $g_{ij}(r)$, and, thus, the rightmost term can be rewritten in terms of these components to give

$$I(q) = S_s(q) + \int_0^\infty 4\pi r^2 [f_C^2(q) c_C^2 g_{CC}(r) + f_C(q) f_N(q) c_C c_N g_{CN}(r) + f_C(q) f_X(q) c_C c_X g_{CX}(r) + f_N^2(q) c_C^2 g_{NN}(r) + f_N(q) f_X(q) c_N c_X g_{NX}(r) + f_X^2(q) c_X^2 g_{XX}(r) + \text{hydrogen-atom terms}] \frac{\sin(qr)}{qr} \, dr \qquad (3)$$

This integral equation cannot be solved using the component RDF's unless the $f(q)$'s are removed from the integral expression. This is typically done by defining an "average" electron structure factor to be

$$f_e(q) = \frac{c_C f_C(q) + c_N f_N(q) + c_X f_X(q) + c_H f_H(q)}{c_C f_C(0) + c_N f_N(0) + c_X f_X(0) + c_H f_H(0)} \qquad (4)$$

Factoring $f_e(q)$ out of the integral and rearranging terms yields the structure function, $H(q)$, such that

$$qH(q) = q\frac{I(q) - S_s(q)}{f_e^2(q)} = \int_0^\infty \text{RDF}(r) \frac{\sin(qr)}{r} \, dr \qquad (5)$$

where RDF(r) is defined to be the radial distribution function. When using the experimental data, $I(q)$ is appropriately scaled so that the structure function goes to zero as $q \to \infty$ by adding and subtracting the mean atomic density, ϱ_0. This gives

$$qH(q) = \int_0^\infty (\text{RDF}(r) - 4\pi r^2 \varrho_0) \frac{\sin(qr)}{r} \, dr + \int_0^\infty 4\pi r^2 \varrho_0 \frac{\sin(qr)}{r} \, dr \qquad (6)$$

The second integral represents scattering from the entire object having a uniform density and is experimentally unobservable. Rearranging terms and Fourier transforming yields the RDF so that

$$\text{RDF}(r) = 4\pi r^2 \varrho_0 + \frac{2r}{\pi} \int_0^\infty qH(q) \sin(qr) \, dq \qquad (7)$$

This result is often expressed in terms of auxiliary functions, $G(r)$ and $W(r)$, described by

$$G(r) = \frac{\text{RDF}(r)}{4\pi r^2 \varrho_0} \qquad W(r) = r(G(r) - 1) \qquad (8)$$

$G(r)$ normalizes the RDF so that, at large r, $G(r)$ approaches unity while $W(r)$ is used either to weight features at larger radius or, when appropriately integrated, to obtain approximate atom−atom coordination numbers.

B. Modeling Analysis. Although modeling analyses of polymer RDF's have been reported,[6,8,9,11,12,50,51] much of the earlier work has focused on simple identifications of the most obvious atom pair distances. The later studies have become much more comprehensive[50,51] as both the quality of the data and analysis have been systematically improved. In this article we have instituted a linked-atom approach to generate model RDF spectra. Ultimately, this enhancement should be extended to include total profile structural refinements in combination with ab-initio molecular modeling techniques.

Comparisons to the experimental data have been made in real space using $G(r)$ or in momentum space using $qH(q)$, the q-weighted structure function. Real-

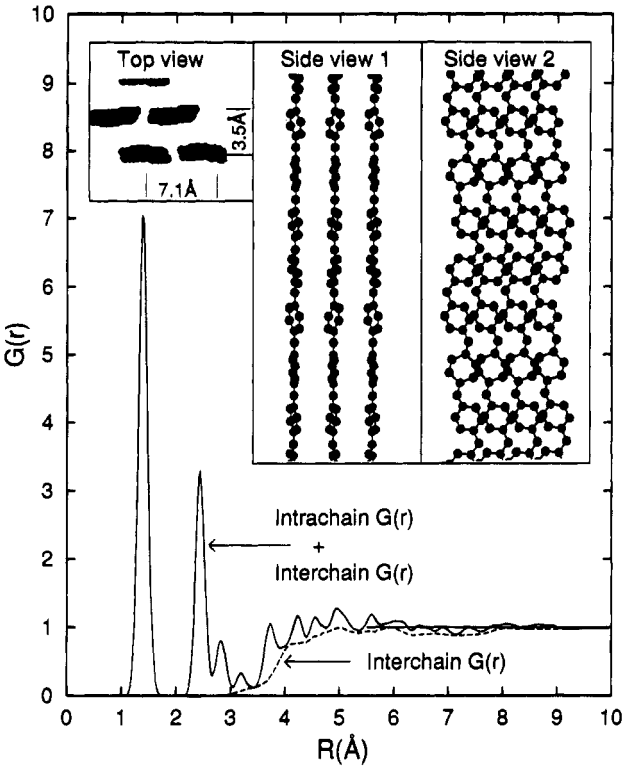

Figure 2. Results for a typical PANI RDF calculation explicitly showing the interchain and total (interchain + intrachain) $G(r)$'s when $\sigma_{\text{interchain}} > \sigma_{\text{intrachain}}$ (see section IV.B) using a base packing structure which is appropriate for crystalline EB (see ref 39). Inset: Three different perspectives of the PANI base structure.

space comparisons enable a more intuitive comparison of the experimental data while q-space comparisons allow for a more straightforward assessment of statistical errors and minimize artifacts introduced during Fourier transformation of experimental data (e.g., see eqn 4). These apparent advantages of the direct q-space comparisons are strongly offset by the existence of systematic errors in the data analysis (e.g., the exact form of the Compton profile) and in the experimental data itself. These effects introduce substantial displacements in the relative position of the experimental curves in relation to those of the calculated profiles.

A trial polymer structure was first generated by using C−C and C−N bond lengths, bond angles, and torsion angles as determined from single-crystal studies of oligomeric PANI.[52,53] These intrachain pair distances are then supplemented by including basic interchain spacings established using the various proposed models for crystalline PANI.[43] Three orthogonal perspectives of this base structure are shown in the inset of Figure 2. To calculate the RDF(r)'s we employ a procedure based on that reported by Billinge et al.[54] for neutron scattering studies of crystalline materials. The nominal RDF profile is given by

$$\mathrm{RDF}(r) = \frac{1}{N}\sum_{\alpha}^{\text{unit cell}}\sum_{\gamma}^{r\le r_{\max}}\frac{f_\alpha(0)f_\gamma(0)}{f_e^{\,2}(0)}\delta(r - r_{\alpha,\gamma}) \quad (9)$$

where the atoms are separated by $r_{\alpha,\gamma} = |\vec{r}_\alpha - \vec{r}_\gamma|$, δ is the Dirac delta function, $f(0)$ is the q = 0 atomic form factor, and N is the number of atoms within an EB unit cell. For these calculations two procedural modifications have been introduced: the hydrogen atoms are lumped together with their nearest carbon or nitrogen neighbor and the cutoff distance, $r_{\max}$, ranges from 9 to 12 Å. Both of these procedures enhance the overall computational speed with some compensating reduction in the overall accuracy. The former modifies the RDF primarily in the 0.5−3.0 Å region and the latter will clearly limit the RDF calculations at the highest radii. The function generated by this last equation is then convoluted with a normalized Gaussian

$$b(r) = \frac{1}{(2\pi)^{1/2}\sigma_c(r)}\exp\left[-\frac{1}{2}\frac{r^2}{\sigma_c^{\,2}(r)}\right] \quad (10)$$

which crudely approximates the uncertainty in atomic positions due to both static disorder and dynamical motion. The standard deviation, σ_c, must be further modified to include more specific features of the experimental apparatus and of the polymer structure itself. Hence,

$$\sigma_c = \sigma_s + \sigma_2 r^2 \quad (11)$$

where $\sigma_2 r^2$ is representative of the experimental resolution[55] and σ_s is related to both intrachain and interchain aspects of the polymer structure. Since each term represents an atom pair,

$$\sigma_s^{\,2} = (\sigma^\alpha)^2 + (\sigma^\gamma)^2 \quad (12)$$

and σ^α and σ^γ imply the uncertainty of the positions of the α,γ atom pair projected onto the vector which connects the two atoms. For intrachain distances, σ is always considered to be isotropic. Pairs that include interchain correlation are considered separately and include displacement parameters which specify positional displacements parallel (z) and perpendicular (ϱ) to the polymer main chains. This gives

$$(\sigma_r^\gamma)^2 = \frac{1}{|r^{\alpha\gamma}|^2}[(r_z^{\alpha\gamma})^2 U_z^\gamma + (r_\varrho^{\alpha\gamma})^2 U_\varrho^\gamma] \quad (13)$$

and introduces axial disorder in a systematic fashion. The calculated RDF is then transformed into $G(r)$ or $W(r)$ for direct comparisons with the experimental data. An example $G(r)$ profile is displayed in Figure 2. In this figure the interchain $G(r)$ profile is also shown explicitly using displacement parameters, U_z^γ and U_ϱ^γ, that produce σ's significantly larger than that specified for the various intrachain pairs. Thus, the interchain $G(r)$ intensity oscillations become more slowly varying.

Alternatively, the structure function, $H(q)$, can be directly determined using the nominal atom pair distributions given in eq 9 and the weighted sum of the partial structure functions $e_{\alpha\gamma}(q)$[11]

$$H(q) = \frac{1}{f_e^{\,2}(q)}\sum_{\alpha,\gamma} f_\alpha(q) f_\gamma(q) e_{\alpha\gamma}(q) \quad (14)$$

where $e_{\alpha\gamma}(q)$ has been separated into intrachain and interchain components. To approximate the intrachain or interchain partial structure functions,

$$e_{\alpha\gamma}(q) = w_{\alpha\gamma}\exp(-l_{\alpha\gamma}^{\,2}q^2/2)\sin(qr_{\alpha\gamma})/(qr_{\alpha\gamma}) \quad (15)$$

where $r_{\alpha\gamma}$ is the mean separation, $l_{\alpha\gamma}$ is the root-mean-square (rms) deviation of this spacing assuming an isotropic distribution, and $w_{\alpha\gamma}$ is the relative number of $\alpha\gamma$ atom pairs. Intrachain and interchain rms values

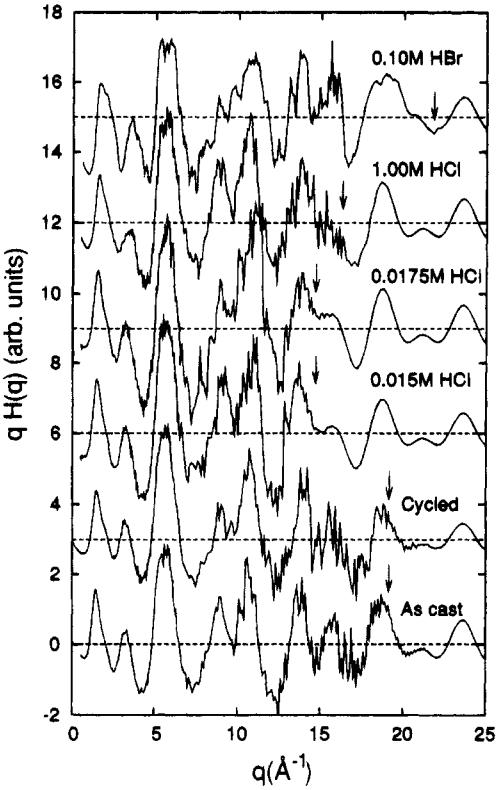

Figure 3. Experimental q-weighted structure functions, $qH(q)$, obtained from the various PANI samples. The low-q regions contain the experimental data while at higher q there is a crossover region (as described in the text and denoted by an arrow) to a representative $qH(q)$ curve obtained from intrachain pair distances restricted to under 3 Å. The 0.10 M HBr curve also contains resolved elastic/Compton data, in the 18–22 Å^{-1} region, which has been extracted directly from the energy dispersive detector output.

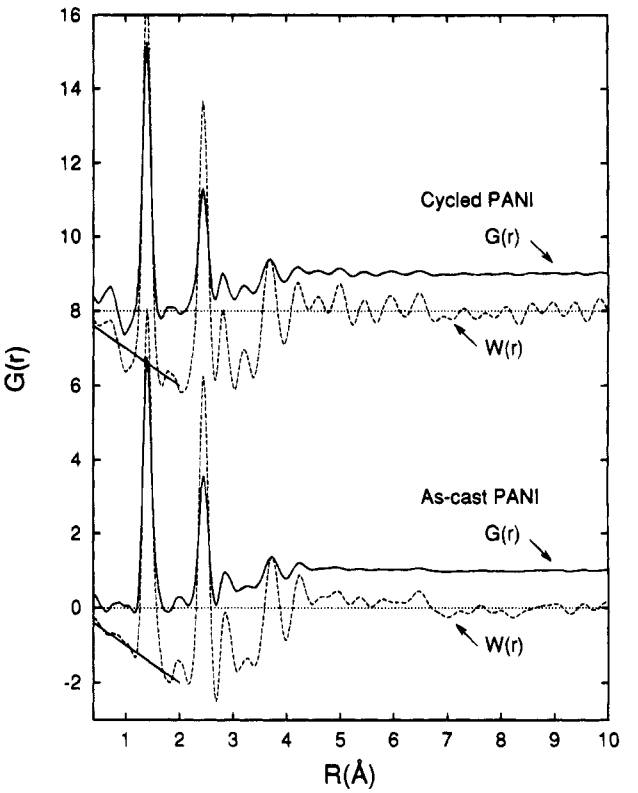

Figure 4. Calculated $G(r)$ and $W(r)$ profiles obtained from the experimental data of as-cast and cycled (doped–undoped) PANI.

are considered separately, but the interchain anisotropy in eq 13 is not included. Once the $H(q)$ is obtained, RDF(r), G(r), and $W(r)$ can all be determined using eqs 7 and 8.

V. Experimental Results and Discussion

A. As-Cast and Undoped PANI. Experimental $qH(q)$ curves are shown in Figure 3 for various PANI samples. In all cases the actual experimental data have been smoothly spliced to a single representative $qH(q)$ curve (as previously described). For one sample, 0.1 M HBr doped PANI, the experimental data could be extended out to 22 Å^{-1} by using the elastic data obtained directly from the energy-dispersive detector. The q-weighted structure functions are always dominated by intensity oscillations arising from interchain pair correlations at low q (typically 5 Å^{-1} or less) while intrachain pair correlations rapidly become important at larger q. From those data it is also apparent that the intensity oscillations extend well beyond 16 Å^{-1} and that improved statistics at these high wave vectors will ultimately be necessary for any comprehensive RDF study of this or any other stiff-backboned polymer.

All of these profiles were then transformed to yield the respective $G(r)$ and $W(r)$ curves. Figure 4 displays the experimental $G(r)$ and $W(r)$ profiles obtained from the as-cast and cycled (HCl doped/NH_4OH undoped) EB samples. Both EB spectra are qualitatively similar to each other and to the analogous RDF spectra reported by Pouget[12] but with appreciably improved resolution and reduced artifacts. In general, the relative RDF intensity fluctuations from our samples at r distances beyond 3.0 Å are noticeably less pronounced than those of ref 12. While this may be an intrinsic effect specific to the details of the polymer film processing, there is evidence that the presence of strong oscillations in $G(r)$ spectra may be artifactual. Significant increases in the magnitude of these intensity oscillations at large r (over 6 Å) can be obtained simply by retaining unprocessed experimental $qH(q)$ data out beyond q = 16 Å^{-1}, i.e., precisely where the statistics are poorest. This systematic behavior is minimized in RDF profiles which are obtained using experimental data that have been restricted to q values of 16 Å^{-1} or less. For these reasons, as well as for comparison purposes, all of the profiles shown in Figure 4 (and also in Figure 7) incorporate data which have been essentially truncated and spliced at or near 16 Å^{-1}.

At the shortest distances, 3 Å or less, the similarity of the various spectra for the two samples is strongest. This region is heavily dominated by the aniline monomer unit pair correlations. Although this result is somewhat influenced by the data analysis described previously, a strong similarity between the as-cast and cycled PANI profiles is still obtained when using a simple, high-q damping of the experimental data. At intermediate distances, up to 5 Å the well-defined chemical architecture of PANI still dominates the RDF profiles so that the two curves in Figure 4 exhibit only slight differences. At larger distances there are modest changes in both the position and relative intensity of various features in the resulting spectra. This latter result is ostensibly consistent with prior observations that dopant cycling can lead to significant irreversible changes in the local structure. However, in striking contrast to the aforementioned RDF results,[12] dopant cycling of our PANI films seems to *intensify* the intensity oscillations in these RDF spectra at the larger r values.

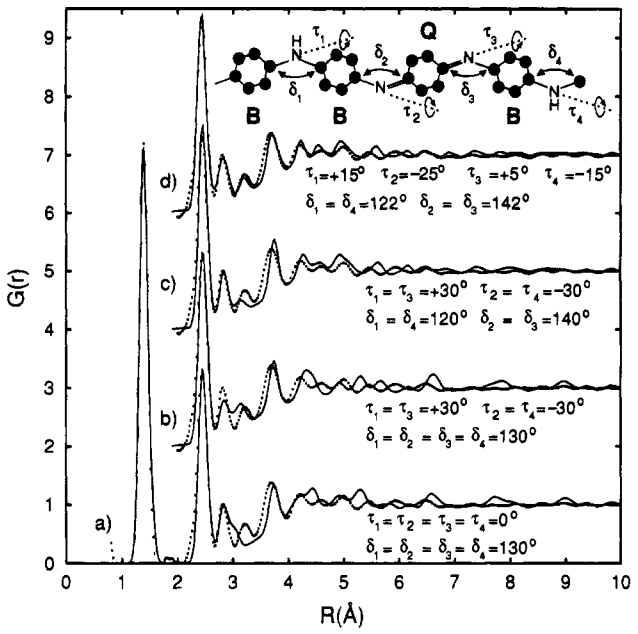

Figure 5. Direct comparison between the experimental (solid lines) and calculated (dotted lines) RDF $G(r)$ profiles using intrachain PANI models with progressively, from a to d, more "realistic" C−N−C bond angles, δ, and phenylene ring torsion angles, τ. Note the torsion angles are referenced to the plane formed by the nitrogen atoms. Inset: Schematic of emeraldine base showing the primary degrees of freedom used in this modeling.

This suggests that halogen acid cycling of PANI may, in some instances, enhance the ordering *within* the amorphous PANI films.

The most pronounced features, at 1.41 and 2.44 Å, arise from nearest-neighbor and next-nearest-neighbor intrachain pair distances. Intensity oscillations at $r \leq 1.4$ Å are generally identified as unphysical artifacts (due to scaling errors) but the weak feature seen near 0.7 Å may, in part, be due to C−H and N−H pair correlations. Another weak RDF feature, centered near 1.8 Å, is usually resolved in our RDF profiles and this may again be artifactual or, alternatively, indicate the presence of impurities and/or dopants in the EB matrix (i.e., H_2O) that have covalently bonded to either carbon or nitrogen atoms.[56] This feature may also be representative of additional H−C or H−N pair correlations. A somewhat surprising feature, not reported in previous RDF studies, is the appearance of two distinguishable peaks at approximately 2.8 and 3.3 Å. This reproducible splitting is *not* resolved in RDF profiles generated from data which have been explicitly truncated at 12 $Å^{-1}$ or less.

All other features, at larger r, must be representative of either intrachain or interchain spacings. The overall complexity of the PANI architecture at r distances beyond 2.5 Å precludes the use of a simple look-up table. Hence, a linked-atom modeling algorithm (described previously) was implemented to test different trial chain conformations. Figure 5 displays the combined intrachain and interchain $G(r)$ spectra for four progressively more "realistic" PANI structures in juxtaposition with the cycled EB sample data. In all instances the interchain rms fluctuations, as specified by an appropriate σ, are substantially larger than those for the intrachain pair correlations. Thus the calculated interchain $G(r)$ forms a slowly varying background and all short-range intensity oscillations in the calculated $G(r)$ arise solely from *intrachain* pair correlations. It is also important to note that the relative intensity scaling between these two components (interchain vs intrachain) is essentially fixed by the equatorial packing density of the model.

The simplest model, seen in the bottom curve Figure 5a, assumes a planar main chain conformation and a uniform 130° C−N−C bond angle. Clearly, there is poor agreement between the two $G(r)$ profiles. Rotating the rings +30° out the plane defined by the nitrogen atoms, shown in Figure 5b, splits the $G(r)$ profile in the vicinity of 3 Å but still yields a poor fit. By allowing for changes in the C−N−C bond angles between amine and imine nitrogens, as in Figure 5c, substantial improvements are realized. Finally, by allowing for slight systematic changes in all bond lengths, bond angles, and torsion angles (shown in Figure 5d), even better agreement can be obtained. This latter model is simply a modified EB structure in which there are three benzenoid rings with modest ring torsions in sequence with a nearly planar quinoidal ring. Similar results can be obtained for the as-cast EB profile using slightly different parameters. The agreement is especially good at distances of less than 5 Å. At larger r values there can be, at times, noticeable deviation but there are also many limiting factors. As stated previously, the specific number of distinguishable peaks and their positions are rather sensitive to the q-value at which data truncation occurs. Subtle variations in our specific fitting procedure produced a variety of modest effects in the resulting $G(r)$. At best, we expect the most pronounced experimental $G(r)$ features at r distances in the range from 2.5 to 8 Å are real (e.g., the peak near 6.5 Å) and near their true position (within ±0.05 Å of the observed value). Our confidence in the position, shape, and/or existence of weaker features in this r range or at distances out beyond 8 Å is somewhat less certain. Table 1 lists the measured peak positions and estimated uncertainties for the as-cast and cycled PANI samples. The model itself is also limited because it is based on a single PANI geometrical construction with relatively few degrees of freedom. Finally, the limited statistics of the raw experimental data strongly impact features at the larger radii. The combination of these factors prevents a full structural refinement at present. Nevertheless, this modeling approach convincingly demonstrates that the RDF analysis may be used to obtain detailed measurements of the local PANI chain conformation. This result is similar to analogous RDF studies of various n-alkanes,[49] model compounds with a far simpler molecular architecture.

Our final model also suggests that these PANI samples are strongly dominated by *intrachain* pair correlations. In retrospect, this result is not unexpected since there is considerable main chain π-conjugation which tends to enforce intrachain ordering over appreciable distances. Calculated RDF profiles in which the intrachain and interchain σ parameters are kept nearly equal always yield unsatisfactory fits to the experimental data. An example comparison, using a reduced interchain σ value, is shown in Figure 6 at center. On this basis we suggest that fully amorphous EB films have an interchain structure which only loosely resembles that of the crystalline phase. RDF studies of partially crystalline nylons[6] also exhibit an absence of well-resolved interchain pair correlations within the amorphous regions.

A final observation is revealed by comparing the "best-fit" model $G(r)$ for the two EB samples displayed. These are also shown in Figure 6 in combination with the

Table 1

as-cast PANI	HCl-cycled PANI	0.015 M HCl PANI	0.0175 M HCl PANI	1.0 M HCl PANI	0.1 M HBr PANI
1.40 ± 0.01[a]	1.40 ± 0.01	1.40 ± 0.01	1.40 ± 0.01	1.40 ± 0.01	1.40 ± 0.01
(1.8)	(1.8)				
2.44 ± 0.02	2.44 ± 0.02	2.44 ± 0.02	2.44 ± 0.02	2.44 ± 0.02	2.44 ± 0.02
2.90 ± 0.05	2.85 ± 0.05	2.88 ± 0.08	2.88 ± 0.08	3.08 ± 0.08	2.88 ± 0.08
3.33 ± 0.10	3.22 ± 0.10				3.41 ± 0.10
3.74 ± 0.05	3.70 ± 0.05	3.59 ± 0.10	3.68 ± 0.10	3.73 ± 0.10	3.74 ± 0.10
4.22 ± 0.05	4.21 ± 0.05	4.25 ± 0.10	4.25 ± 0.10	4.21 ± 0.10	4.13 ± 0.10
4.56 ± 0.10	4.56 ± 0.05	4.70 ± 0.10	4.61 ± 0.10	4.55 ± 0.10	4.54 ± 0.10
4.93 ± 0.10	5.00 ± 0.05	5.16 ± 0.10	5.18 ± 0.10	5.02 ± 0.10	5.14 ± 0.10
5.30 ± 0.10	5.47 ± 0.05			5.47 ± 0.10	5.55 ± 0.10
5.70 ± 0.10	5.93 ± 0.05	5.76 ± 0.10	5.83 ± 0.10	5.93 ± 0.10	5.99 ± 0.10
6.42 ± 0.05	6.49 ± 0.05	6.35 ± 0.10	6.38 ± 0.10	6.55 ± 0.10	6.43 ± 0.10
		6.93 ± 0.10	6.89 ± 0.10	7.07 ± 0.10	6.79 ± 0.10
7.22 ± 0.10	7.30 ± 0.10				
7.60 ± 0.10	7.68 ± 0.10	7.48 ± 0.10	7.48 ± 0.10	7.45 ± 0.10	7.36 ± 0.10
8.02 ± 0.10	8.07 ± 0.10	7.97 ± 0.10	7.94 ± 0.10	7.81 ± 0.10	7.82 ± 0.10
8.6 ± 0.2	8.6 ± 0.2	8.5 ± 0.2	8.5 ± 0.2	8.3 ± 0.2	8.2 ± 0.2
9.0 ± 0.2	9.0 ± 0.2	8.8 ± 0.2	9.0 ± 0.2	8.8 ± 0.2	8.7 ± 0.2
9.5 ± 0.2	9.4 ± 0.2	9.4 ± 0.2	9.5 ± 0.2	9.2 ± 0.2	9.3 ± 0.2
10.0 ± 0.2	9.8 ± 0.2	9.9 ± 0.2		9.7 ± 0.2	9.8 ± 0.2

[a] In angstroms.

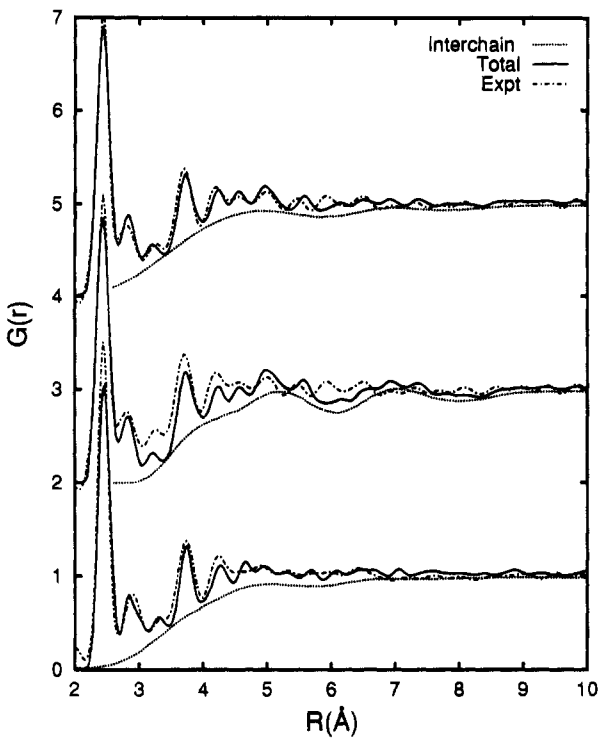

Figure 6. Top: Offset profiles of "best-fit" model $G(r)$ (total $G(r)$ (solid line) and interchain $G(r)$ (dotted line)) in comparison with experimental $G(r)$ (dot–dash line) for cycled PANI sample using $\sigma_{\text{interchain}} \approx 0.25$ Å ($U_z = 0.25$ Å and $U_Q = 2.0$ Å) and $\sigma_{\text{intrachain}} = 0.08$ Å. Middle: Same curves as at top except $\sigma_{\text{interchain}} = 0.08$ Å. Bottom: Comparison of "best-fit" model $G(r)$ (total $G(r)$ (solid line) and interchain $G(r)$ (dotted line)) in comparison with experimental $G(r)$ (dot–dash line) for as-cast PANI sample using $\sigma_{\text{interchain}} \approx 0.15$ Å and $\sigma_{\text{intrachain}} = 0.08$ Å.

respective experimental data. To match the slowly varying $G(r)$ interchain curve in the 3–5 Å regime, it is necessary to employ appreciably larger interchain U_z and U_r parameters for the cycled sample. Our tentative conclusion is that dopant cycling effects an increase in the distribution of nearest-neighbor interchain distances with only minimal variations in the mean spacing. An increased distribution implies that some chain pairs pack more tightly while other chain pairs move further apart. This behavior is consistent with recent gas sorption studies[57] of films which find only a slight increase in the monomer molar volume during cycling (from 276 to 282 cm^3/mol-repeat unit) while gas diffusion studies find dramatically increased permeability in cycled EB films.[17]

Interestingly, we simultaneously observe both an increase in the RDF intensity oscillations at large radius, 4.5 Å and higher, and an increase in the magnitude of the interchain disorder parameters needed for an overall fit. This suggests a competition between the intrachain and interchain ordering whereby modest local enhancements of the intrachain structure may be achieved only by measurably altering the surrounding interchain pair correlations. Additional studies are clearly necessary to further substantiate this claim.

B. HBr- and HCl-Doped PANI. Five ES samples are discussed in this section. Although doping initiates dramatic changes in the local bond order, all doped samples yielded nearly identical RDF peaks at 1.41 and at 2.44 Å. This is, once again, expected because of the limited q-range experimentally accessible and by the explicit termination methods employed herein. Figure 7 contains expanded $G(r)$ profiles spanning from 2 to 10 Å from four of these ES[58] in combination with data from the two EB samples. A complete summary of the various observed peak positions is listed in Table 1. The various curves in Figure 7 have been organized so that arrows can be used to specify the sequential halogenic acid processing procedure. The molar halogen acid concentrations have been chosen to closely follow those used in ref 17. Halogen acid concentrations of 1–4 M typically yield $y \approx 0.50$ ES while 0.015–0.0175 M solutions yield $y \approx 0.25$.[59] It is also important to note that the 0.015 and 0.0175 M HCl redoped samples utilized the same cycled PANI film whereas the 0.1 M HBr, 1.0 M HBr, and 1.0 M HCl treated samples employed different pristine as-cast EB films.

Direct qualitative comparisons of the various samples are revealing. For instance, the intensity oscillations in the $G(r)$ profile from the 1 M HCl treated sample more closely follow those of the cycled sample (in the range 3.5–8.0 Å) than those of the as-cast film. This suggests that any enhancement in the local intrachain PANI structure occurs during the initial doping cycle. Undoping does not cause significant reorganization of the intrachain structure except for the loss of dopant and restoration of the EB $(B-B-Q-B-)_n$ repeat.

Further comparisons using the two HCl redoping profiles are also instructive. Since the dopant concen-

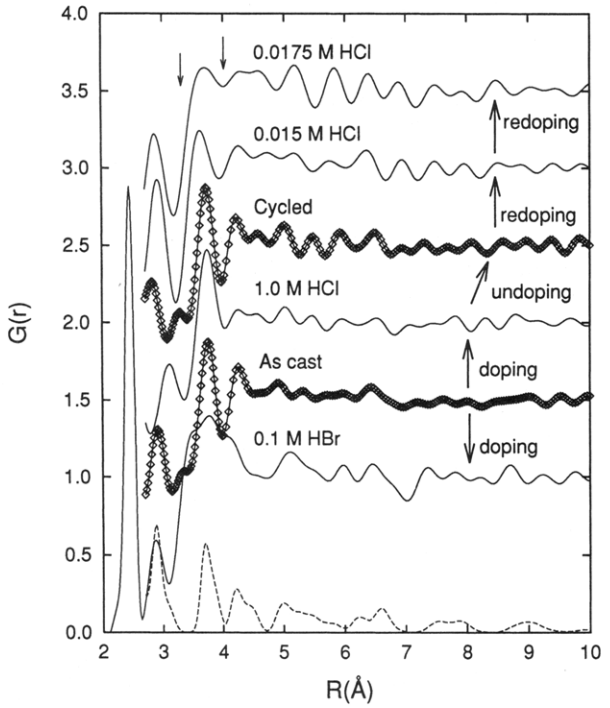

Figure 7. Calculated $G(r)$ profiles obtained from the experimental data of various EB and ES PANI samples shown in Figure 3. For comparison purposes, all of these $G(r)$ curves use $qH(q)$ data which have been spliced to the representative high-q model (see text) curve at q-values near 16 Å^{-1}. These spectra have been offset for clarity and so that the heavy arrows may be used to identify a typical processing sequence. The bottom-most curve is an intrachain-only $G(r)$ profile for a single PANI chain with a uniform C−N−C bond angle of 130° and alternating ring torsion angles of ±10°.

tration changes only slightly between the 0.015 and 0.0175 M redoped samples, these two spectra are expected to be very similar. The pertinent $G(r)$ curves in Figure 6 show good reproducibility with respect to the actual number of peaks resolved and the overall functionality. However, specific peak positions and relative peak intensities do vary somewhat. These variations, especially at the larger distances, are attributed to the limitations in the experimental data. Surprisingly, these HCl-redoped PANI profiles are, in the region from 5 to 8 Å, noticeably different from that of either the cycled sample or the 1.0 M HCl treated sample. Hence there may be additional evolution of the PANI molecular structure during additional doping cycles. Alternatively, this may indicate the presence of an intermediate structural ordering.

Universal differences between doped ES and dopant-free EB RDF profiles are also evident. The most obvious of these is the appearance of only a single distinguishable peak at a radius intermediate to the 2.8−3.2 Å "pair" characteristic of EB samples. Nominally, this result is indicative of changes in the PANI short-range order but, since doping also involves inclusion of halogen ions, halogen−PANI and halogen−halogen RDF components are also a distinct possibility. The effective area under this single peak is more consistent with pair correlations arising solely from intrachain pairs. Hence, the first significant halogen−PANI pair spacing within these samples appears to occur at distances beyond that appropriate for covalent halogen atom bonding to the PANI chain.[11] It is straightforward, using changes in the local intrachain structure (as seen in Figure 4) to significantly alter the form and position of the weak feature centered near 3.2 Å and simultaneously modify the position of the 2.8 Å peak in various model calculations. We are able to simulate the $G(r)$ line shape in this region for all but one of the doped PANI $G(r)$ spectra. The exception occurs for the 1 M HCl doped sample, which exhibits an anomalously large shift in this peak position to 3.06 Å.

Systematic $G(r)$ variations are also observed in the region spanning from 3.0 to 4.5 Å. All ES samples exhibit a more abrupt onset of a rapid $G(r)$ intensity increase in the vicinity of 3.4 Å and, simultaneously, a reduction in the $G(r)$ intensity dip centered at 4.0 Å. These features are indicated in Figure 7 by the thin arrows. In the case of the 0.10 M HBr doped sample, these features are even more pronounced. Since Br scatters more strongly than Cl, this implies that halogen−PANI atom pair correlations are partially resolved in these $G(r)$ profiles. Finally, the overall peak intensity of the peak centered near 3.75 Å is found to be strongly sample dependent and, relatively speaking, most pronounced in the as-cast and cycled emeraldine base films. If one refers back to the model $G(r)$ profiles shown in Figure 4, then it is readily seen that the PANI intrachain RDF peak centered about 3.75 Å is effectively model *independent*. Because of this intrachain characteristic and because the halogen−PANI pair correlations will generally only introduce new or enhanced $G(r)$ peaks, the observed relative intensity loss at this r distance (within the various doped samples) is evidence for significant changes within the local *interchain* structure.

There are a myriad of factors which must be fully considered before a comprehensive model and an associated RDF spectrum are obtained. These include changes in the local intrachain PANI structure, changes in the PANI interchain structure, and the addition of both halogen−PANI and halogen−halogen atom pair correlations. The doped PANI films may also contain substantial mole weight fractions of water. A complete accounting for all these effects represents a major challenge for these modeling calculations and, given the current limitations of these data, is still beyond the scope of this approach. However, a somewhat more restricted treatment is possible.

Since the overall PANI electron density is only mildly increased by Cl or Br doping,[57] a single idealized *intrachain*-only $G(r)$ profile (shown at the bottom of Figure 7) which faithfully reproduces the single 2.9 Å peak profile may be first generated, then appropriately scaled, and finally subtracted from the individual HCl or HBr acid doped PANI $G(r)$ profiles. These "partial" $G(r)$ curves qualitatively represent a combination of halogen−PANI and interchain RDF contributions. The specific model used for the aforementioned $G(r)$ curve in Figure 7 employs a uniform 130° C−N−C bond angle and alternating phenylene ring torsions of ±10°. The resulting difference curves for the various samples are displayed in Figure 8. In all cases the nearly featureless *interchain* $G(r)$ curves appropriate for modeling the as-cast and undoped EB films become inadequate because all these $G(r)$ difference curves exhibit well-resolved RDF peaks near 3.5 and 4.1 Å. These features must be a combination of well-defined halogen−C or halogen−N pair distances and systematic changes in the interchain RDF. There is also evidence for a much weaker feature near 3.8 Å. Additional peaks at 4.7 and 5.4 Å are also consistently obtained but these features are found to be extremely sensitive to the attributes of the specific intrachain model employed prior to the simple subtrac-

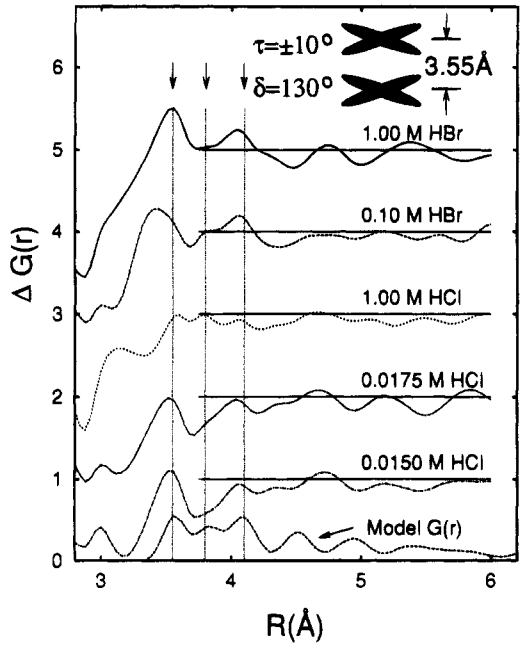

Figure 8. Difference $G(r)$'s obtained by scaling and subtracting out the model intrachain $G(r)$ (shown at the bottom of Figure 7) from the experimental ES $G(r)$ profiles. The dashed curve at the bottom is an interchain-only $G(r)$ which has been obtained by using a pair of PANI chains which have an interchain packing as depicted in the inset. The vertical lines (and arrows) identify the new, reproducible features near 3.5, 3.8, and 4.1 Å that are indicative of structural changes in the interchain packing. All curves have been offset for clarity.

tion procedure.

We again note that the relative intensity dip seen in the 3.75 Å region cannot be achieved through the presence of additional halogen–PANI RDF contributions. Therefore it must originate from changes in the *interchain* PANI structure. Furthermore, the base PANI–PANI interchain packing used for modeling of the undoped films (as shown in the inset of Figure 2) generates an interchain RDF which also cannot account for this net reduction in peak intensity at 3.75 Å. Halogen acid doping must also systematically change the local PANI interchain packing structure. Since these changes are most pronounced in the 3.5–4.2 Å region, a cooperative interchain phenylene ring ordering process must be invoked.

One possible interchain packing which qualitatively reproduces the major new features in these $G(r)$ difference profiles is also displayed in Figure 8 (at bottom). This calculated curve is simply the interchain $G(r)$ profile obtained by using just two PANI chains which have been configured back-to-back (see the inset of Figure 8). This packing configuration is also common to crystalline ES.[39] We note that at no time do we observe evidence for crystalline domain formation in our films. Hence this packing would extend over an extremely limited number of PANI chain pairs. The overall functionality of this model agrees rather well with the experimentally derived profiles in the critical 3.5–4.2 Å range. It is still difficult at this stage to obtain an estimate of the exact X–PANI (X = Cl, Br) pair spacings. However, the disproportionately larger changes which accompany the HBr-doped PANI sample spectra (in the 3–5 Å region) suggest that well-defined Br–PANI pair correlations do exist and occur at or near 3.4, 3.9, and 5.2 Å.

In order to integrate this new interchain packing structure into a comprehensive total profile fitting scheme, it will be necessary to introduce a model that differentiates between neighboring phenylene units that are well ordered and those that are not. Furthermore, the overall shape of the interchain profile is extremely sensitive to the packing both parallel and perpendicular to the polymer chain axis. This sensitivity may be correlated with the high degree of sample-to-sample variability as observed in the 3–5 Å region.

C. A Molecular Model. From these results a speculative structural scenario can be devised which self-consistently describes the subtle interplay between PANI interchain and intrachain ordering processes and also provides a possible mechanism by which halogenic acid processing may systematically alter the PANI microstructure. This then leads to an intuitive picture that relates these changes in the local structure to the observed variations in the mass diffusion properties.

Initially, amorphous as-cast EB films exhibit a very disordered structure in which there are few well-defined interchain pair distances. The existence of this highly disordered state may be related to the specifics of the processing (i.e., time, temperature, and solvent) or, alternatively, there may be an intrinsic packing "frustration" that is caused by structural inhomogeneities within individual chains of the emeraldine base polymer (i.e., varying phenylene ring torsions and the approximate 20° C–N–C imine/amine bond angle alternation). In any case, the experimental RDF profiles in these samples are dominated by intrachain pair correlations that correspond to pair distances within and between neighboring aniline monomer units.

After protonation (i.e., doping) this highly disordered EB state is replaced by a more homogeneous structure along individual PANI chains so that the C–N–C bond angle alternation and ring torsion angles typical of the pristine host are significantly diminished. In support of this we note that single-crystal studies of heavily doped PANI oligomers report a nearly uniform C–N–C bond angle.[52,53] Enhanced intrachain structural regularity enables a finite proportion of the phenylene rings to repack more closely, thereby enhancing nearest-neighbor interchain ordering. In order to pack specific PANI chains more closely, other nearby PANI interchain pairs would have to move further apart. This would necessarily create somewhat larger gaps in the PANI host matrix and would also be expected to facilitate the dopant uptake.

The net result is that, on undoping, the nominal $(B–B–Q–B)_n$ intrachain EB structure is recovered but there are irreversible changes in the local structure. It is likely that an appreciable fraction of those areas which developed enhanced intrachain and interchain ordering are partially retained after undoping. Since this structural relaxation is a local process, it is likely that PANI chains which exhibit the best interchain ordering are also immediately surrounded by regions that contain the largest nearest-neighbor interchain spacings.

Subsequent redoping, by halogenic acids, would preferentially target those sites with the largest nearest-neighbor interchain pair spacings. From a structural perspective one can reasonably argue that sites with the largest effective pore size are most easily accessed. However, the extreme selectivity of this process on redoping is hard to justify on these grounds alone.

One possibly important component of this behavior may relate to the electroactive nature of PANI and the existence of microscopic regions which contain enhanced

intrachain and interchain structural ordering. Improved intrachain ordering and interchain packing are both associated with an increase in the overall π-conjugation length of the polymer chain. Both of these processes are also responsible for shifts in the various electronic states to lower energy. Other conducting polymers, such as polyacetylene, are well-known to preferentially dope regions which have the longest conjugation lengths.[60] Because of this proximity between the closest and furthest packed chains, dopant sites that bind most effectively are immediately surrounded by chains with the largest nearest-neighbor interchain spacing. Once these specific sites become occupied, continued doping occurs at less energetically favorable sites and so on. This then forms the electronic basis for the high site specificity on doping. The subsequent stepwise reduction in the effective pore size is then mirrored in the very precise size selectivity seen on redoping.

VI. Conclusions

A combination of RDF analysis and structural modeling has been used to more fully investigate the halogenic acid doping-induced changes in the molecular ordering within PANI films. The results for EB samples are particularly encouraging because both the intrachain and interchain RDF's can be individually distinguished and modeled. In either as-cast or cycled EB samples, all of the well-defined RDF features can be attributed only to intrachain pair correlations. All interchain pair correlations effectively form a smoothly varying background. The results for the acid-doped samples are similarly revealing but somewhat less certain. In general, these data support a model in which there are systematic changes in both the intrachain and interchain structural ordering.

If the intriguing model proposed in section V.C is accepted, then one can suggest avenues which may further enhance the PANI film properties or the design of other electroactive materials for use as separation membranes. One may be able to simply optimize the processing of the as-cast films and the resultant microstructure so that a greater proportion of the film volume is rendered active after halogen acid treatment. Specific chemical substitutions of the dopant or base monomer may provide a straightforward means for altering the physical, chemical, and/or electroactive response of processed polymer films so that certain key functionalities are optimized. In all these cases it appears that the electroactive nature of the host polymer is prerequisite for the formation of these high-performance films.

Although these results presented in the paper are significant, they must be viewed as cursory. The current limitations to this modeling approach reside solely in the quality and quantity of available data. Hence, there are many key aspects within these structures that remain unresolved, especially at distances beyond 5 Å. For instance, the precise location of the halogen ions within the polymer host is still an open question and, as yet, no accounting for the presence of water molecules has been made. Still the RDF method has been shown to be a powerful and direct probe of polymer structure.

Acknowledgment. The financial support by NSF DMR Grant No. DMR-8917530 (J.M. and M.J.W.) and DOE AIM Program (B.R.M.) is gratefully acknowledged. We would like to thank David Cox, T. Egami, and the Brookhaven National Laboratory NSLS for their support of the X7A beamline and technical assistance. We also appreciate informative discussions with S. Billinge and acknowledge R. Kaner for his assistance in the earliest stages of this study.

References and Notes

(1) Robeson, L. M. *J. Membr. Sci.* **1991**, *62*, 165.
(2) Alexander, L. E. *X-ray Diffraction Methods in Polymer Science*; Wiley-Interscience: New York, 1969.
(3) Warren, B. E. *X-ray Diffraction*; Addison-Wesley: Reading, MA, 1969.
(4) Klug, H. P.; Alexander, L. E. *X-ray Diffraction Procedures for Polycrystalline and Amorphous Materials*; Wiley-Interscience: New York, 1974.
(5) Mitchell, G. R. In *Comprehensive Polymer Science*; Allen, G., Bevington, J. C., Booth, C., Price, C., Eds.; Pergamon: Oxford, 1989; Vol. 1, p 687.
(6) Narten, A. H.; Habenschuss, A.; Xenopoulos, A. *Polymer* **1991**, *32*, 1923.
(7) Windle, A. H. *Pure Appl. Chem.* **1985**, *57*, 1627.
(8) Mitchell, G. R.; Lovell, R.; Windle, A. H. *Polymer* **1992**, *23*, 1273.
(9) Narten, A. H. *J. Chem. Phys.* **1989**, *90*, 5857.
(10) Cai, H.; Hu, R.; Egami, T.; Farrington, G. C. *Solid State Ionics* **1992**, *52*, 333.
(11) Annis, B. K.; Narten, A. H.; MacDiarmid, A. G.; Richter, A. F. *Synth. Met.* **1988**, *22*, 191.
(12) Laridjani, M.; Pouget, J. P.; Scherr, E. M.; MacDiarmid, A. G.; Jozefowicz, M.; Epstein, A. J. *Macromolecules* **1992**, *25*, 4106.
(13) Laridjani, M.; Pouget, J. P.; MacDiarmid, A. G.; Epstein, A. J. *J. Phys. I* **1992**, *2*, 1003.
(14) Smith, P. J. C.; Arnott, S. *Acta Crystallogr., Sect. A* **1978**, *34*, 3.
(15) Busing, W. R. *Macromolecules* **1990**, *23*, 4068.
(16) Carotenuto, M.; Iannelli, P. *Macromolecules* **1992**, *25*, 4373.
(17) Anderson, M. R.; Mattes, B. R.; Reiss, H.; Kaner, R. B. *Science* **1991**, *252*, 1412.
(18) See, for example, the *Handbook of Conducting Polymers*; Skotheim, T., Ed.; Dekker: New York, 1986; Vols. 1 and 2 or the most recent International Conference on Synthetic Metals proceedings (see *Synth. Met.* **1993**, *55–57*).
(19) Heeger, A. J.; Schriefer, J. R.; Su, W.-P. *Rev. Mod. Phys.* **1988**, *40*, 3439.
(20) Tsukamoto, J. *Adv. Phys.* **1992**, *41*, 509.
(21) Genies, E. M.; Boyle, A.; Laplowsi, M.; Tsintavis, C. *Synth. Met.* **1990**, *36*, 139.
(22) Cao, Y.; Andreatta, A.; Heeger, A. J.; Smith, P. *Polymer* **1989**, *30*, 2305.
(23) Armes, S. P.; Miller, J. F. *Synth. Met.* **1988**, *22*, 385.
(24) Oh, E. J.; Min, Y.; Wiesinger, J. M.; Manohar, S. K.; Scherr, E. M.; Prest, P. J.; MacDiarmid, A. G.; Epstein, A. J. *Synth. Met.* **1993**, *55*, 977.
(25) MacDiarmid, A. G.; Chiang, J. C.; Halpern, M.; Huang, W. S.; Mu, S. L.; Somasiri, N. L. D.; Wu, W.; Yaniger, S. I. *Mol. Cryst. Liq. Cryst.* **1985**, *121*, 173.
(26) Huang, W. S.; Humphrey, B. D.; MacDiarmid, A. G. *J. Chem. Soc., Faraday Trans.* **1986**, *82*, 2385.
(27) MacDiarmid, A. G.; Epstein, A. J. *Mater. Res. Soc. Symp. Proc.* **1990**, *173*, 293.
(28) Heeger, A. J.; Smith, P. In *Conjugated Conducting Polymers*; Keiss, H. G., Ed.; Springer-Verlag: New York, 1992; Vol. 102, p 141.
(29) Andreatta, A.; Tokito, S.; Moulton, J.; Smith, P.; Heeger, A. J. In *Science and Applications of Conducting Polymers*; Salaneck, W. R., Clark, D. T., Samuelsen, E. J., Eds.; Adam Hilger: Bristol, 1991; p 105.
(30) MacDiarmid, A. G.; Epstein, A. J. In *Science and Applications of Conducting Polymers*; Adam Hilger: Bristol, 1991; p 141.
(31) MacDiarmid, A. G.; Chiang, J. C.; Richter, A. F.; Epstein, A. J. *Synth. Met.* **1987**, *18*, 285.
(32) Epstein, A. J.; Ginder, J. M.; Zuo, F.; Bigelow, R. W.; Woo, H. S.; Tanner, D. B.; Richter, A. F.; Huang, W. S.; MacDiarmid, A. G. *Synth. Met.* **1987**, *18*, 303.
(33) Mattes, B. R.; Anderson, M. R.; Reiss, H.; Kaner, R. B. *Polym. Mater. Sci. Eng.* **1991**, *64*, 336.
(34) Anderson, M. R.; Mattes, B. R.; Reiss, H.; Kaner, R. B. *Synth. Met.* **1991**, *41*, 1151.
(35) Mattes, B. R.; Anderson, M. R.; Reiss, H.; Kaner, R. B. *Synth. Met.* **1993**, *55*, 3655.
(36) Chiang, J. C.; MacDiarmid, A. G. *Synth. Met.* **1986**, *13*, 193.

(37) Ray, A.; Richter, A. F.; MacDiarmid, A. G.; Epstein, A. J. *Synth. Met.* **1989**, *29*, E151.
(38) Stafstom, S.; Bredas, J. L.; Epstein, A. J.; Woo, H. S.; Tanner, D. B.; Huang, W. S.; MacDiarmid, A. G. *Phys. Rev. Let.* **1987**, *59*, 1464.
(39) Jozefowicz, M. E.; Laversanne, R.; Javadi, H. H. S.; Epstein, A. J.; Pouget, J. P.; Tang, X.; MacDiarmid, A. G. *Phys. Rev. B* **1989**, *39*, 12958.
(40) Wudl, F.; Angus, J.; Lu, F. L.; Allemand, P. M.; Vachon, D. J.; Nowak, M.; Liu, Z. X.; Heeger, A. J. *J. Am. Chem. Soc.* **1987**, *109*, 3677.
(41) Kaplan, S.; Conwell, E. M.; Richter, A. F.; MacDiarmid, A. G. *Macromolecules* **1989**, *22*, 1669.
(42) Wang, Z. H.; Ray, A.; MacDiarmid, A. G.; Epstein, A. J. *Phys. Rev. B* **1991**, *43*, 4373.
(43) Pouget, J. P.; Jozefowicz, M. E.; Epstein, A. J.; Tang, X.; MacDiarmid, A. G. *Macromolecules* **1991**, *24*, 779.
(44) Fischer, J. E.; Tang, X.; Scherr, E. M.; Cajipe, V. B.; MacDiarmid, A. G. *Synth. Met.* **1991**, *41*, 661.
(45) Scherr, E. M., et al. *Synth. Met.* **1991**, *41*, 735.
(46) This is not true of the 3 Å (or so) crossover region at high q where the experimental data are spliced to the calculated RDF profile.
(47) Cromer, D. T.; Mann, J. B. *J. Chem. Phys.* **1967**, *47*, 1893.
(48) Krogh-Moe, J. *Acta Crystallogr.* **1956**, *9*, 951.
(49) Narten, A. H.; Habenschuss, A. *J. Chem. Phys.* **1990**, *92*, 5692.
(50) Mitchell, G. R.; Rosi-Schwartz, B. *Physica B* **1992**, *180*, 558.
(51) Rosi-Schwartz, B.; Mitchell, G. R.; Soper, A. K. *Physica B* **1992**, *180*, 561.
(52) Shacklette, L. W.; Wolf, J. F.; Gould, S.; Baughman, R. H. *J. Chem. Phys.* **1988**, *88*, 3955.
(53) Baughman, R. H.; Wolf, J. F.; Eckhardt, H.; Shacklette, L. W. *Synth. Met.* **1988**, *25*, 121.
(54) Billinge, S. J. L.; Egami, T. *Phys. Rev. B* **1993**, *47*, 14386.
(55) Almenningen, A.; Bastiansen, O.; Fernholt, L.; Cyvin, B. N.; Cyvin, S.; Samdal, S. *J. Mol. Struct.* **1985**, *128*, 59.
(56) PANI, especially when in its salt form, can be hygroscopic. The actual water concentration may reach 50 mol wt % (i.e., one water molecule per every two phenylene rings).
(57) Mattes, B. R., unpublished.
(58) Data from the fifth sample, 1.0 M HBr treated PANI, extended to only 12 $Å^{-1}$ and are not included in Figure 7.
(59) Even significant errors in the assumed composition do not negatively influence the RDF calculations because of the scaling corrections introduced in the RDF analysis procedure.
(60) Schen, M. A.; Lefrant, S.; Perrin, E.; Chien, J. C. W.; Mulazzi, E. *Synth. Met.* **1989**, *28*, D287.

MA946202V